Absorption-limited and phase-matched high harmonic generation in the tight focusing regime

Jan Rothhardt[1,2], Manuel Krebs[1], Steffen Hädrich[1,2], Stefan Demmler[1], Jens Limpert[1,2] and Andreas Tünnermann[1,2,3]

[1] Institute of Applied Physics, Abbe Center of Photonics, Friedrich-Schiller University Jena, Albert-Einstein-Straße 15, D-07745 Jena, Germany
[2] Helmholtz-Institute Jena, Fröbelstieg 3, D-07743 Jena, Germany
[3] Fraunhofer Institute of Applied Optics and Precision Engineering, Albert-Einstein-Straße 7, D-07745 Jena, Germany
Email: j.rothhardt@gsi.de

Abstract

High harmonic generation (HHG) at a high repetition rate requires tight focusing of the moderate peak power driving pulses. So far the conversion efficiencies that have been achieved in this regime are orders of magnitude behind the values that have been demonstrated with loose focusing of high energy (high peak power) lasers. In this contribution, we discuss the scaling laws for the main physical quantities of HHG and in particular analyze the limiting effects: dephasing, absorption and plasma defocusing. It turns out that phase-matched and absorption-limited HHG can be achieved even for very small focal spot sizes using a target gas provided with an adequately high density. Experimentally, we investigate HHG in a gas jet of argon, krypton and xenon. By analyzing the pressure dependence we are able to disentangle the dephasing and absorption effects and prove that the generated high order harmonics are phase-matched and absorption-limited. The obtained conversion efficiency is as high as 8×10^{-6} for the 17th harmonic generated in xenon and 1.4×10^{-6} for the 27th harmonic generated in argon. Our findings pave the way for highly efficient harmonic generation at megahertz repetition rates.

1. Introduction

High harmonic generation (HHG) represents a unique method for generating coherent short wavelength radiation (XUV to soft x-ray) and ultrashort attosecond pulses [1, 2]. Optimized generation conditions enable conversion efficiencies up to 4×10^{-5} into the 15th harmonic of a 40 fs, 1.5 mJ Ti:sapphire laser [3]. Achieving such efficiencies requires phase matching of the driving nonlinear polarization with the generated high harmonics and a sufficiently high number of coherent emitters, hence, a high density-length product of the target within the interaction region. While Ti:sapphire lasers can provide high photon numbers per pulse at correspondingly low repetition rates (typically 10 Hz up to a few kHz), some applications require high harmonic sources with orders of magnitude higher repetition rates. For example, photoelectron spectroscopy on solid surfaces requires a low number of photons per pulse in order to minimize space charge effects [4]. The same requirement holds for coincidence detection of charged particles after photoionization, where less than one ionization event per laser shot is required [5]. These applications call for the highest possible repetition rate that can be processed by the employed detectors, which can be as high as several MHz.

Novel laser concepts, employing Yb-based gain materials and advanced geometries of the active medium, such as disk [6], slab [7] and fiber [8], nowadays permit high repetition rate femtosecond lasers with average output powers approaching and even exceeding 1 kW. Such lasers have the potential of increasing the repetition rate of HHG sources by orders of magnitude and, therefore, advance the above-mentioned applications. In addition, the average photon flux of the HHG source can be increased by orders of magnitude. Hence, photon-hungry applications such as coherent diffractive imaging [9] will benefit from these powerful, coherent short wavelength sources as well.

The first attempts towards high repetition rate HHG sources have been undertaken with Ti: sapphire lasers at a 100 kHz repetition rate, and resulted in a very low conversion efficiency ($<10^{-9}$) [10]. Since then, a number of groups reported experiments on high repetition rate HHG employing different laser architectures [11–18]. Although a variety of generation conditions have been explored, the obtained conversion efficiencies have been rather poor in all of these experiments, ranging from $\sim 10^{-8}$ at a 100 kHz repetition rate [11] to below 10^{-10} at megahertz repetition rates [14, 16]. This was attributed to the 'extremely small interaction volume' [10] and lack of phase matching [11] caused by the tight focusing of the generating lasers.

A numerical optimization recently revealed conditions for phase-matched HHGs in this tight focusing regime [19] and a conversion efficiency as high as 5×10^{-7} has been achieved for H11 to H19 employing a 1.03 μm driving laser and a xenon gas cell target. More generally, Heyl *et al* investigated the scaling of phase matching with the focal diameter [11]. They found that tight focusing requires very high target pressures in order to achieve phase matching. In addition, geometrical scaling considerations unveiled that, if the experiment is scaled correctly and the required phase matching pressure can be provided, the conversion efficiency should, in principle, be independent of the focal diameter [11].

In this contribution we extend the considerations on HHG in a tight focusing geometry to the all-important physical quantities involved in the HHG process. We derive a set of scaling

Table 1. Scaling relations of the coordinates and physical quantities.

Coordinate		
Longitudinal z	$z' =$	$z*s^2$
Transversal x	$x' =$	$x*s$
Transversal y	$y' =$	$y*s$
Quantity		
Wavelength	$\lambda' =$	λ
Pulse duration	$\tau' =$	τ
Incident intensity	$I'(x', y', z') =$	$I(x, y, z)$
Pulse energy	$E_1' =$	E_1*s^2

laws that allow a comparison of the physics at loose and tight focusing. Particular emphasis is put on the efficiency-limiting effects: dephasing, absorption and plasma defocusing. Furthermore, we analyze how the required target density can be achieved technically. Experimentally, we investigate phase matching and absorption effects in a tight focusing geometry employing a high-pressure gas jet target. Our experimental investigations enable disentangling of dephasing and absorption effects, which gives detailed insight into the generation conditions. Finally, we conclude that high order harmonics are generated as phase-matched and absorption-limited in our configuration. The resulting conversion efficiency of 8×10^{-6} for H17 is, to our knowledge, the highest that has ever been achieved with tight focusing.

2. Theory: scaling of HHG with a focal spot diameter

The process of HHG requires a certain intensity, I, which is of the order of $10^{14}\,\mathrm{W\,cm^{-2}}$ depending on the target gas and the harmonic order to be generated. Hence, the laser peak power will determine the required focal spot radius, w_0. In the following sections we will discuss how the physics of HHG scales with this beam radius. We assume Gaussian beam optics within the paraxial approximation, which is justified if $w_0 > 1.22\lambda$ [20], with λ being the driving laser wavelength. The corresponding Rayleigh-range is $z_0 = \pi w_0^2/\lambda$. Since we want to compare the physics of tightly focused HHG (beam radius w_0) with the well explored loose focusing regime (beam radius $w_0' \gg w_0$), we introduce the following scaling parameter as the ratio of the beam radii:

$$s = w_0'/w_0. \tag{1}$$

As a result of Gaussian optics, this leads to the following transformation between original (x) and scaled quantities (x'). The transversal coordinates x and y scale linearly with s, while the longitudinal coordinate z scales quadratically with s, and so does the Rayleigh-range. All geometrical quantities follow these scaling laws. The same single atom response of the generation medium is achieved by assuming the same intensity distribution $I(x, y, z)$, laser wavelength λ and pulse duration τ. Consequently, the required pulse energy of the driving laser scales quadratically with s. Table 1 summarizes the scaling relations of all coordinates and important physical quantities. This set of scaling relations is equivalent to the scaling considerations that have been derived by Heyl *et al* in [11] with respect to the focal length f of

the employed focusing element. In the following subsections it will allow investigation of all the important quantities for HHG.

2.1. Phase matching

Phase matching of the laser-induced polarization and the generated high order harmonics is required for efficient buildup along the propagation direction within the generation medium. The wave vector mismatch between laser-induced polarization and the generated high order harmonics in a free focusing geometry is generally governed by three contributions: Δk_{Gouy}— the geometrical wave vector mismatch caused by focusing, $\Delta k_{\text{Dispersion}}$—due to the dispersion of the generating medium and free electrons, and Δk_{Dipole}—due to the intensity dependent dipole phase [21]. The first term is caused by the Gouy phase and calculates as:

$$\Delta k_{\text{Gouy}} = q \frac{\partial \varphi_{Gouy}}{\partial z} = q \frac{\partial}{\partial z}\left(-\arctan\left(\frac{z}{z0}\right)\right). \tag{2}$$

The dispersive term consists of two contributions originating from the neutral atoms and the free electrons [22], which cause wave vector mismatch with the opposite sign. It can be calculated by the following equation:

$$\Delta k_{Dispersion} = \frac{2\pi q}{\lambda} \frac{p}{p0} \Delta\delta\left(1 - \frac{\eta}{\eta_c}\right). \tag{3}$$

Here, q is the harmonic order, $\Delta\delta$ is the difference of the refractive indices of the fundamental and high order harmonic, p_0 is the standard pressure (1013 mbar), η is the ionization fraction and η_c is the critical ionization fraction, which is reached when plasma dispersion of the free electrons exceeds the atomic dispersion [23]. Note that the dispersive term scales linearly with the pressure of the target gas p. Hence, at a given focusing geometry, phase matching can be achieved by adjusting the gas pressure until the dispersion of the generating medium compensates for the Gouy phase and the dipole phase. The latter can be well approximated by:

$$\Delta k_{Dipole} = -\alpha_q \frac{\partial I}{\partial z}, \tag{4}$$

with the proportional constant α_q being positive for the short trajectories [21]. As pointed out by Heyl *et al* in [11], within the laser focus, Δk_{Dipole} equals zero and the phase matching pressure p at the position of the laser focus can be calculated as:

$$p = p_0 \frac{\lambda^2}{2\pi^2 w_0^2 \Delta\delta\left(1 - \frac{\eta}{\eta_c}\right)}. \tag{5}$$

It can be seen that the higher the ionization fraction, the higher the phase matching pressure. Once the ionization fraction reaches the critical ionization η_c, perfect phase matching is no longer possible. Note that the ionization fraction evolves with time and perfect phase matching is only transiently achieved within a real laser pulse. Nevertheless, an important scaling law for the phase matching pressure, which has been introduced by Heyl *et al* [11], can be extracted from equation (5). The phase matching pressure scales inversely with the square of
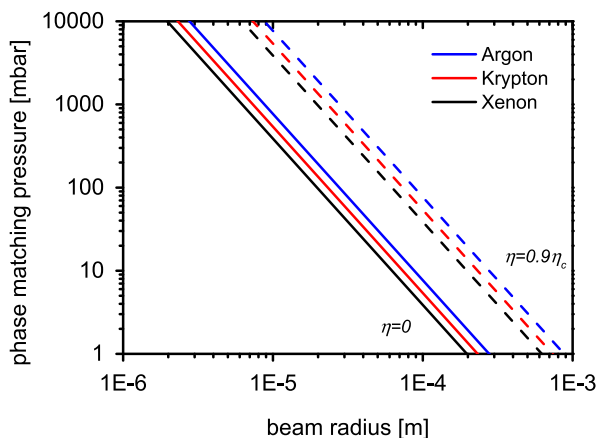
Figure 1. Calculated phase matching pressure versus beam radius w_0 for H17 and $\lambda = 820$ nm employing argon (blue), krypton (red) and xenon (black) as the generating medium. The dispersion properties of the gases have been taken from [24].

the beam radius w_0, as does the Gouy-phase gradient. Hence, tight focusing requires large pressures (or densities) in the interaction region in order to achieve phase matching.

Figure 1 displays the calculated phase matching pressure p versus the beam radius w_0 for H17 and $\lambda = 820$ nm. While loose focusing ($w_0 > 100 \, \mu$m) results in a phase matching pressure in the mbar range, tight focusing ($w_0 = 10 \, \mu$m) requires a phase matching pressure of nearly 1 bar for negligible ionization ($\eta = 0$) and reaches 10 bar for $\eta = 0.9 \, \eta_c$ in the case of argon. Due to higher dispersion, krypton and xenon require slightly lower backing pressures.

In practice, the gas jet position is chosen to be slightly behind the laser focus in order to favor phase matching of the short trajectories [20]. Compared to the situation in focus, the Gouy-phase gradient decreases. Furthermore, the dipole phase helps to balance the wave vector mismatch due to focusing in this case. Consequently, a slightly lower phase matching pressure will be required.

2.2. Scaling of the conversion efficiency

The overall harmonic energy E_h generated by a single laser pulse with the energy E_l along the propagation axis can be calculated by the following relation [22, 25]:

$$E_h \sim \left(p l_{\max} \right)^2 d_{\max}{}^2. \tag{6}$$

Here, $l_{\max}$ and $d_{\max}$ characterize the length and the diameter of the generating volume, within which the intensity is high enough to generate a particular harmonic. Table 2 summarizes the scaling relations required for calculating the harmonic flux. It can be seen that the scaling of the phase matching pressure and medium length compensate for each other. Hence, the pressure length product for phase-matched HHG is invariant on the geometrical scaling. Furthermore, both harmonic energy and the driving laser energy scale quadratically with s. Note that this scaling has also been obtained by Heyl *et al* [11] by employing very similar considerations. As a result, the conversion efficiency is also invariant on geometrical scaling, provided that the pressure is increased accordingly.

Table 2. Scaling relations of the conversion efficiency and related quantities.

Quantity		
Medium length	$l_{max}' =$	$l_{max} * s^2$
Medium diameter	$d' =$	$d * s$
Pressure	$p' =$	$p\, s^{-2}$
Pressure length product	$p' * l_{max}' =$	$p * l_{max}$
Harmonic energy	$E_h' =$	$E_h * s^2$
Driving laser energy	$E_l' =$	$E_l * s^2$
Conversion efficiency	$\eta' =$	η

2.3. Limiting factors for HHG: absorption, dephasing and defocusing

The conclusions of the previous subsection are based on equation (6), which does not take potentially limiting effects, such as absorption, dephasing and defocusing, into account. These effects will now be discussed separately.

Reabsorption of generated high harmonic photons in the generation medium limits the conversion efficiency of HHG. The so-called absorption limit is reached with a phase-matched generating medium longer than $3l_{abs}$ [3], with the absorption length $l_{abs} = 1/\sigma\rho$. Here, σ is the absorption cross section and ρ the target gas density. Consequently, the absorption length scales as $l_{abs} = l_{abs} \cdot s^2$. Since absorption length l_{abs} and medium length l_{max} scale equally, absorption effects are invariant to scaling with s.

Dephasing of the laser-induced polarization and the generated high order harmonics limits the coherent buildup along the propagation direction z to the coherence length $l_{coh} = \pi/\Delta k$. Note that the phase matching considerations, given in section 2.1, are strictly only valid for a particular spatial coordinate and one certain time within the laser pulse. Due to the spatial intensity distribution and the accumulation of ionization, a certain space and time-dependent wave vector mismatch Δk can be present. It is important to note that the intensity and consequently the ionization fraction at a certain time t scale according to $I'(x', y', z') = I(x, y, z)$ and $\eta'(x', y', z') = \eta(x, y, z)$. Hence, $\Delta k_{Dispersion}$ scales with s^{-2} along the optical axis, such as Δk_{Dipole}, which is proportional to dI/dz. As a result, the longitudinal component of the wave vector mismatch follows the following relation: $\Delta k'(x', y', z') = \Delta k(x, y, z)\, s^{-2}$. Due to the scaling law of the longitudinal coordinates, the accumulated phase mismatch along the optical axis is equal before and after application of the scaling transformation: $\Delta\varphi'(x', y', z') = \Delta\varphi(x, y, z)$. In the paraxial approximation, this also holds true for small off-axis angles. Thus, the coherent buildup is invariant on the proposed scaling with s.

Defocusing of the driving laser reduces the intensity and thus the single atom response. It is caused by a refractive index gradient induced by stronger ionization in the center of the laser beam. The refractive power θ_x of a small slice of the medium with a length of Δz is given by:

$$\theta_x(x, y, z) = \frac{1}{f_x(x, y, z)} = -\frac{\partial^2 n(x, y, z)}{\partial x^2}\Delta z. \tag{7}$$

The refractive power θ_y is calculated analogously. In consequence, considering the scaling laws for longitudinal lengths and the refractive index distribution, the focal length f of each slice scales as:
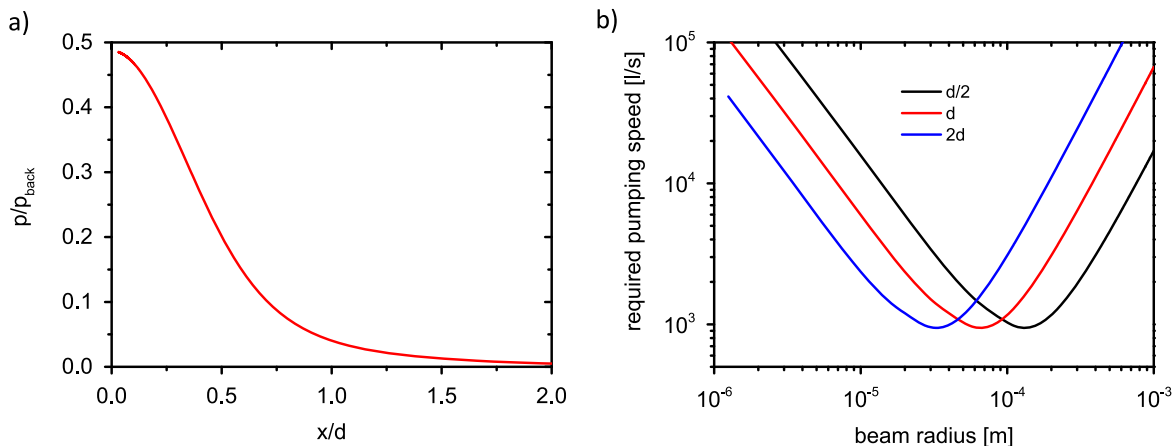
a)

b)

Figure 2. (a) Centerline pressure p normalized to the backing pressure p_{back} versus relative distance x/d (d, diameter of jet). (b) The calculated pumping speed required to maintain a residual pressure of 10^{-2} mbar in the vacuum chamber for a phase-matched HHG experiment scaled with the beam radius for different nozzle diameters ($d/2$, d and $2d$).

$$f'_{x/y}(x', y', z') = f_{x/y}(x, y, z)\, s^2. \tag{8}$$

Thus, the focal lengths at all locations and times and, consequently, all optical imaging properties, scale exactly as all other geometrical lengths in the z-direction. Hence, the impact of defocussing is also invariant on the proposed scaling.

In summary, all the effects that potentially limit the efficiency of HHG scale accordingly with the scaling laws introduced above. Consequently, in the frame of the presented theory, the physics and, in particular, the conversion efficiency is found to be invariant to scaling of the beam radius. Thus, HHG in the tight focusing regime should allow for conversion efficiencies similar to the ones obtained for loose focusing if the target density (pressure) in the interaction region is increased accordingly.

2.4. High-density target for tight focusing HHG

Tight focusing leads to HHG in a smaller, but equally denser medium and should theoretically result in the same conversion efficiency, provided that the high phase matching pressure (high target density) can be achieved. It has been claimed previously that technical constraints, in particular the throughput of the vacuum pumping system, hinder this experimentally [11, 19]. Starting from the experimental setup used by Constant *et al* [3] (laser beam radius $w_0 = 125\,\mu m$, jet diameter $d = 800\,\mu m$ and phase matching pressure $p_{pm} \sim 100$ mbar) we investigate how the gas load to the vacuum system scales with the laser beam radius by employing the above-presented scaling laws. For the following considerations we assume an ideal supersonic gas jet emerging from a round orifice with the diameter d as the target. The gas flow into the chamber is proportional to the product of the backing pressure and the area of the opening into the chamber [26].

In addition, the ratio of the distance to the nozzle opening x and jet orifice diameter d determines the fraction of backing pressure, which is found in the interaction region. This ratio, displayed in figure 2(a), is determined by the jet expansion and calculated via the analytical fit

functions given in [26]. We assume the center of the laser beam to be as close as $x = 2w_0$ to the nozzle opening. The required jet diameter d scales linearly with the medium length l_{max}, hence, quadratically with s.

Consequently, the ratio x/d scales with s^{-1}. Figure 2(b) displays the calculated pumping speed of the vacuum system that would be required to maintain a backing pressure of 10^{-2} mbar in the experimental chamber. For large laser beam diameters ($d > 100 \mu$m) x/d is very small ($\ll 0.1$) and the ratio p/p_{back} is nearly constant. Hence, an approximately quadratic scaling of the required pumping speed is observed in this case. For small laser beam diameters, x/d increases and therefore p/p_{back} decreases rapidly. Hence, the backing pressure p_{back} has to be increased much stronger than the required phase matching pressure p and the gas load to the vacuum chamber increases. Interestingly, the required pumping speed behaves differently in the two regimes when the diameter of the jet orifice is changed, as illustrated in figure 2, for three different relative orifice diameters, d (red), $d/2$ (black) and $2d$ (blue). In the case of loose focusing, doubling the orifice increases the gas load by roughly a factor of four. Consequently, gas cell targets are typically employed if very large beam diameters are used. In contrast, for tight focusing the gas load can be reduced if a larger orifice is used, hence, a larger fraction of the backing pressure is found in the interaction region due to a reduced jet expansion (smaller x/d).

Note that a rectangular gas jet with the longer dimension oriented parallel (perpendicular) to the propagation direction of the driving laser can be utilized for reducing the gas load in case of loose (tight) focusing, respectively. Hence, our investigations, in contrast to the current opinion found in many publications [11, 19], show that the phase matching pressure for HHG can be achieved with gas jets even in the tight focusing regime, at least for beam radii between 10 and 100 μm. For much smaller focal spots, not only do many of our approximations break down, but other physical limitations might also arise, such as clustering effects [27]. At extremely high pressures, the electron excursion distance approaches the mean free path length, which potentially reduces the efficiency and coherence of the HHG process. For example, at $I = 10^{14}$ W cm^{-2} and $\lambda = 1 \mu$m, the spatial electron excursion is as large as 2.9 nm, which equals the mean free path length in xenon at 12 bar.

3. Experiment: absorption-limited HHG with tight focusing

The considerations and calculations presented in section 2 of this paper have shown that for HHG in tight focusing conditions, in principle, it should be feasible to achieve a conversion efficiency similar to what has been obtained with loose focusing. The following section describes a series of experiments that demonstrate both phase-matched and absorption-limited HHG despite tight focusing. The driving laser system is a high repetition rate few-cycle laser system based on optical parametric amplification [28]. The laser system delivers ∼8 fs pulses at an 820 nm central wavelength and 150 kHz repetition rate. An $f = 75$ mm off-axis parabola is employed as the focusing element in order to avoid chromatic and spherical aberrations. The beam radius in the focus $w_0 = 15 \mu$m allows peak intensities of up to ∼2×10^{14} W cm^{-2} with 6.5 μJ measured on target. The target gas (argon, krypton or xenon) for HHG is provided by a 150 μm diameter cylindrical nozzle backed with up to 9 bar of pressure. A 1300 l s^{-1} turbo-molecular pump is employed in order to keep the residual pressure in the vacuum chamber below 10^{-2} mbar. A spectrometer (Ultrafast Innovations), equipped with a gold-coated variable line spacing flat-field grating (nominal 1200 lines mm^{-1}) and a XUV-sensitive charge-coupled
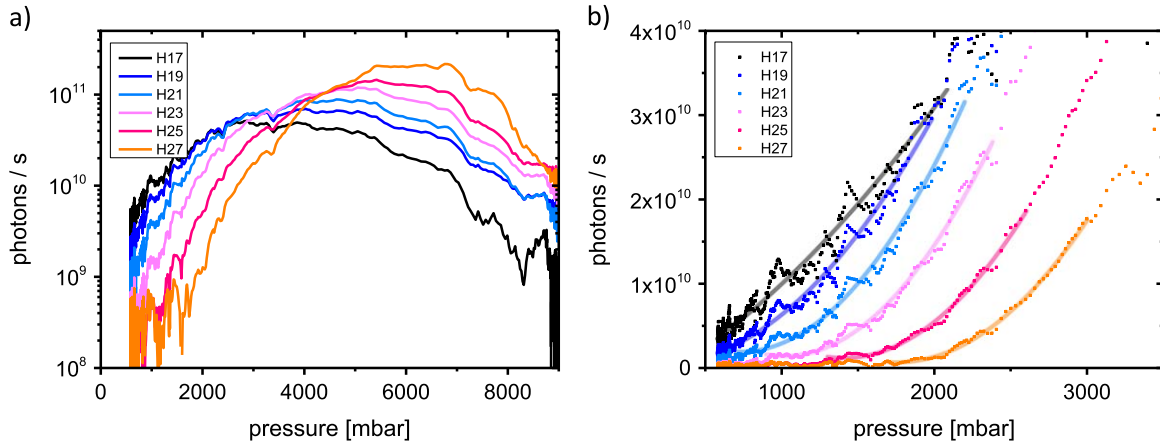
Figure 3. (a) Measured photon flux generated in argon versus applied backing pressure, (b) measured photon flux (dots) and the corresponding quadratic fit function (lines).

device (CCD) camera, is utilized for spectral and spatial characterization of the generated high order harmonics. The spectrometer has been configured to detect the spectral range of H17 to H27, although even higher orders might have been generated. The fundamental radiation of the driving laser is blocked by a 200 nm thick aluminum filter. Synchronized recording of the backing pressure and the harmonics spectra allows for detailed investigations on the pressure dependence of HHG in our configuration.

By placing the gas jet slightly behind the focus of the driving laser, short trajectories have been selected and optimized for the highest on-axis harmonic emission [29]. The photon count rate for each individual harmonic has been obtained by summing over the divergent spatial coordinate and the spectral width of the harmonic line. The generated photon flux is calculated by accounting for the measured transmission of a 200 nm Al-filter, the diffraction efficiency of the spectrometer grating and the efficiency of the CCD detector. Note that the grating efficiency has been determined by calculations calibrated to measurements obtained at a synchrotron with a precision of ±25% [22].

The evolution of the recorded harmonic signal generated in argon with the backing pressure is displayed in figure 3. The harmonics have been generated with a peak intensity of $\sim 1.7 \times 10^{14}$ W cm^{-2}. The resulting ionization fraction in the pulse peak, calculated according to ADK ionization rates [30], is as low as 1.5% while the critical ionization fraction is $\eta_{crit} = 5\%$ for H17.

Figure 3(b) displays the measured photon flux on a linear scale (dots) together with the corresponding quadratic fit functions (lines). Note that a quadratic growth, which is expected if the macroscopic conditions do not change significantly, is obtained for small backing pressures, but a saturation followed by a decrease of the generated harmonic signal is obtained when the backing pressure is further increased. The backing pressure required for the maximum photon count increases with the harmonic order. While H17 peaks at $\sim$3 bar, H27 requires $\sim$6.5 bar to be maximized. Moreover, H27 is generated most efficiently. The peak photon flux is as high as 2.2×10^{11} photons s^{-1}, which corresponds to a conversion efficiency of 1.4×10^{-6}. Remarkably, this value is very close to the 3×10^{-6} that has been obtained with similar laser pulses and loose focusing and identified to be limited by linear absorption [31].

Our results can be well explained by reabsorption of the generated harmonics within and behind the generation volume. Since the absorption cross section of argon is as high as 32 Mbarn (1 Mbarn $= 10^{-18}$ cm^2) at H17, but decreases to only 3.4 Mbarn at H27 [32], H27 is generated most efficiently and peaks at the highest backing pressure ($\sim$7 bar). Note that, at pressures higher than 7 bar, a rapid drop of H27 is observed which might be due to dephasing or defocusing, which affects the highest harmonic orders most severely.

Similar pressure scans have been recorded with krypton and are displayed in figure 4. The peak intensity has been reduced to $\sim$1.4$\times$10^{14} W cm^{-2} with a neutral density filter wheel in order to keep the calculated ionization fraction at the peak of the laser pulse as low as 4.7% despite the lower ionization potential. Again, a quadratic growth is obtained at low pressure (see figure 4(b)). Compared to argon, the peaks of the harmonic signals are obtained at lower pressure with weaker dependence on the harmonic order. When the backing pressure is further increased, the low harmonic orders decrease steadily. In contrast, the high orders show a clear minimum followed by regrowth of the signal and a second decrease. Such a periodic structure indicates changes in the phase matching conditions and is usually referred to as a Maker fringe [33, 34]. The first minimum clearly marks conditions where harmonics are generated in one part of the interaction region and interfere destructively with equally strong harmonics generated in a second part of the interaction region, i.e. $l_{\text{med}} = 2l_{\text{c}}$.

Additionally, we investigated HHG in xenon. In this case, the peak intensity has been reduced to $\sim$1$\times$10^{14} W cm^{-2}. The calculated ionization fraction at the peak of the laser pulse is 12%, and slightly exceeds the critical ionization fraction (9.5% for H17). Hence, the phase-matched fraction of the pulse will be located before the peak. The measured pressure dependence of the harmonic flux for xenon is displayed in figure 5(a). Again, a quadratic dependence at low pressures is observed (see figure 5(b)). At higher pressures, very clear Maker fringes including multiple minima are observed. Since $\Delta k_{\text{Dispersion}}$ depends linearly on the target gas pressure (see equation (3)), these fringes provide rich information on the pressure dependence of the wave vector mismatch for each individual harmonic order. In particular, a wave vector mismatch equal to $\Delta k = n \cdot (2\pi/l_{\text{med}})$ will result in a characteristic minimum in the pressure scan. Figure 6(a) displays the pressure dependence of the intensity for H21, which has been recorded on-axis (blue). For comparison, the function sinc^2($\Delta k * l_{\text{med}}/2$), which describes the influence of wave vector mismatch on the harmonic intensity, has been plotted (black). Note that the minima are equidistantly separated by $\Delta k = 2\pi/l_{\text{med}}$. However, at $\Delta k = 0$ a maximum is found instead of a minimum, which allows non-ambiguous assignment of a corresponding wave vector mismatch to each minimum. Figure 6(b) displays the pressure and the correspondingly assigned wave vector mismatch for H17 to H25.

A linear fit now allows the determination of the coherence length l_{coh} relative to the medium length l_{med} for each harmonic order at each pressure. Moreover, it allows measurement of the phase matching pressure ($\Delta k = 0$) for each harmonic (H17: $p = 1.9$ bar, H19: $p = 1.6$ bar, H21: $p = 1.5$ bar, H23: $p = 1.3$ bar, H25: $p = 1.0$ bar). This method represents a unique characterization of the phase matching conditions for HHG. Its accurateness is given by the precision the minima can be detected with in the experimental pressure scan, which is about ±10% for the presented experiment.

A striking feature that can be observed from the presented measurements in xenon is that the high order harmonics are most efficiently generated at a pressure significantly higher than the phase matching pressure. For example, H25 peaks at $\sim$1.5 bar, while the phase matching pressure is only $(0.98 + -0.1)$ bar. In this case the coherence length is calculated to be
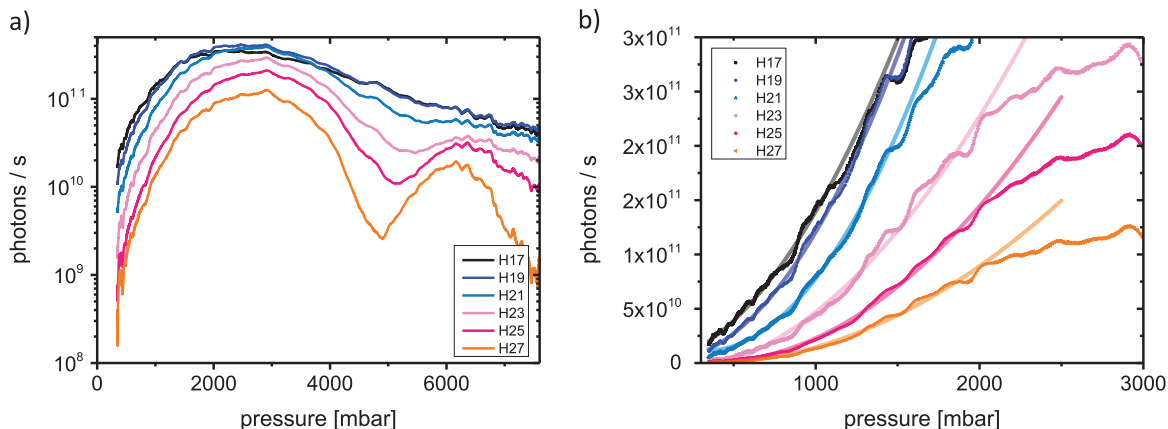
Figure 4. (a) The measured photon flux generated in krypton versus the applied backing pressure, (b) measured photon flux (dots) and the corresponding quadratic fit function (lines).
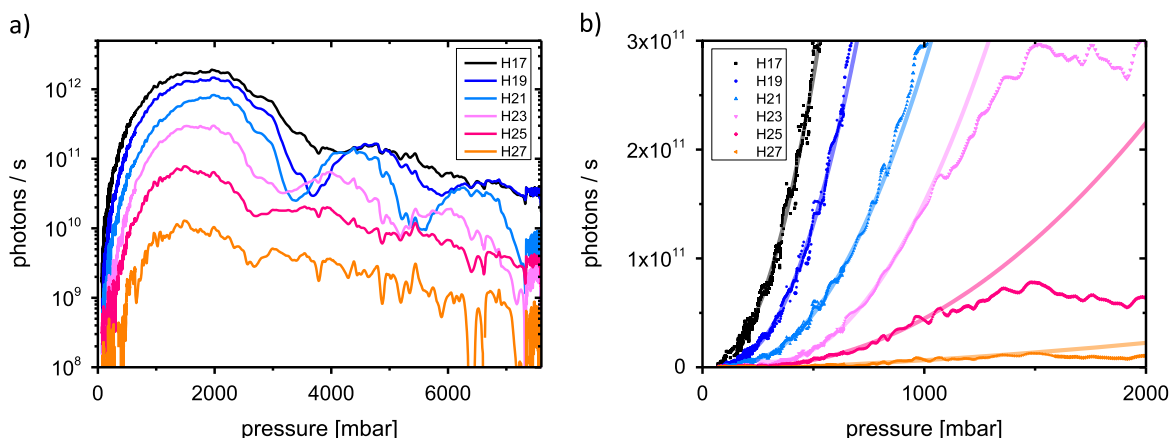

Figure 5. (a) The measured photon flux generated in xenon versus the applied backing pressure, (b) measured photon flux (dots) and the corresponding quadratic fit function (lines).

$l_{\mathrm{coh}} = 1.85 l_{\mathrm{med}}$. Hence, a slight wave vector mismatch is present, but the harmonic signal is increased by the higher number of coherent emitters due to an increased target density. In contrast, the signal of the low order harmonics peaks at pressures only slightly higher than the perfect phase matching pressure. The different behavior can be attributed to absorption effects due to a strongly increasing absorption cross section of xenon at low photon energies [35]. The relative height of the neighboring maxima in the pressure scan for the different harmonic orders supports this statement. The low orders, in particular H17, are strongly absorbed with increasing pressure.

Calculations of the gas expansion (see section 2.4.) give a measure of the target density in the interaction region. At 2 bar backing pressure we find 800 mbar in the interaction region. The resulting absorption length is 1.5×10^{-5} m for H17. Therefore, the length of the generating medium l_{med}, which for the low harmonic orders is given by the gas jet diameter (150 μm), is much larger than the absorption length ($l_{\mathrm{med}} > 10 l_{\mathrm{abs}}$ for H17). In addition, from the linear fits
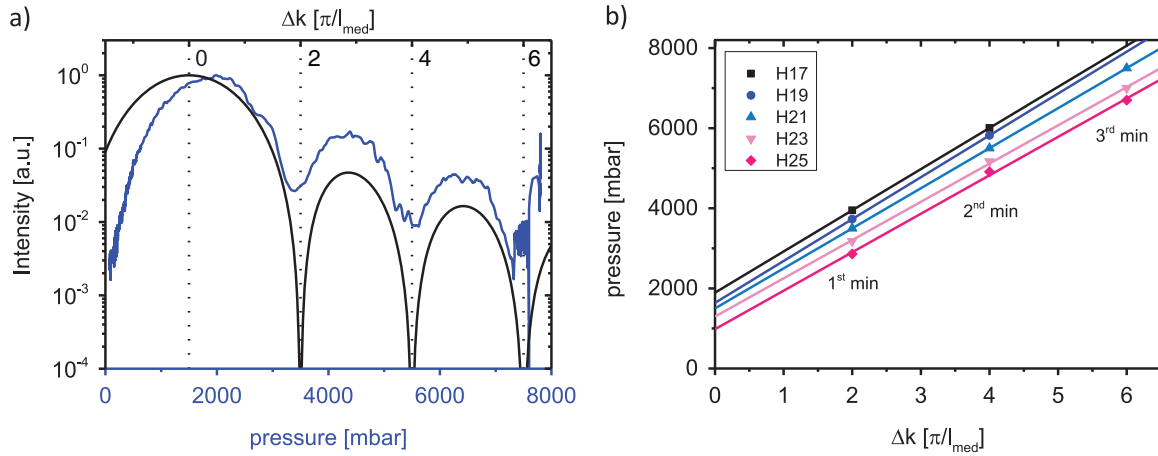
Figure 6. (a) Normalized harmonic intensity versus backing pressure for H21 measured on-axis (blue) and the corresponding $\mathrm{sinc}^2(\Delta k * l_{\mathrm{med}}/2)$ function describing the influence of wave vector mismatch on the harmonic intensity (black). (b) Backing pressure measured for all minima observed in the xenon pressure scan versus the assigned wave vector mismatch (dots) and corresponding linear-fit functions (lines).

displayed in figure 6(b) we can determine the coherence length for H17 at two bar backing pressure to be as large as $l_{\mathrm{coh}} = 10 l_{\mathrm{med}}$. Hence, both conditions for high-efficiency HHG are fulfilled: $l_{\mathrm{med}} > 3 l_{\mathrm{abs}}$ and $l_{\mathrm{coh}} > 5 l_{\mathrm{abs}}$ [3]. Thus, we conclude that H17 is generated phase-matched and absorption-limited in our configuration. Indeed, the conversion efficiency that has been achieved in xenon is as high as 8×10^{-6} for H17. This is the highest efficiency ever obtained with tight focusing HHG and close to the benchmark value of $2 \cdot 10^{-5}$ that has been reported for H15 in a xenon gas jet under optimized loose focusing conditions [3].

Note that at conditions optimized for the generation of H17, the residual xenon pressure in the vacuum chamber is as high as 1.9×10^{-2} mbar. With the measured photoionization cross section of xenon given in [35], the calculated transmission up to the detector is $\sim 65\%$ for H17. Moreover, much higher gas densities are likely to be present close to the gas jet, but have not been measured or precisely modeled so far. Certainly, reabsorption can be further reduced and efficiencies even closer to the theoretical absorption limit will be reached in future with optimized nozzle geometries and vacuum systems.

4. Conclusion

The physics of HHG in the tight focusing regime have been investigated both theoretically and experimentally. A thorough theoretical analysis of the main physical quantities of HHG suggests that phase-matched and absorption-limited HHG can be achieved even for very small focal spot sizes. Furthermore, our analysis predicts that the conversion efficiency of HHG in the tight focusing regime can be similar to what has been obtained with loose focusing of millijoule-class lasers, if the target gas is provided with sufficiently high density.

A proof of principle experiment has been performed with a high repetition rate few-cycle laser system. Despite tight focusing, we achieved high conversion efficiencies of 8×10^{-6} for H17 in xenon and 1.4×10^{-6} for H27 in argon. By recording the HHG spectrum over a large

range of backing pressures we were able to disentangle dephasing and absorption effects, and prove that the generated high order harmonics are phase-matched and absorption-limited.

The utilized laser system has been operated at 150 kHz for the experiments presented herein. It has already been demonstrated that the repetition rate of this laser system can be increased up to 1 MHz with similar pulse parameters [28]. Moreover, well controlled generation of isolated attosecond pulses has recently been demonstrated at high repetition rates with the same laser architecture [36]. Hence, a multi-megahertz repetition rate high harmonic source providing more than 10^{12} photons s^{-1} and isolated attosecond pulses seems clearly in reach. Applications in surface science [4], but also photoionization and dissociation studies based on coincidence measurements [5], would benefit from such an XUV source.

Moreover, our findings can be applied to any HHG experiment requiring tight focusing, including HHG in passive enhancement cavities [37], HHG inside laser oscillators [38] and single pass HHG at high repetition rates. In particular, HHG with high average power femtosecond lasers such as thin disk oscillators [6], slab [7] and fiber [8] amplifiers will allow extraordinarily high photon flux approaching 1 mW average power per harmonic. Further scaling is expected by employing a coherent combination of multiple amplifiers in the driving laser [39]. Thus a new class of ultra-high photon flux HHG sources will be available and enable seminal studies such as multidimensional and time-resolved diffractive imaging or optical coherence tomography [40] in future.

Acknowledgments

References

[1] Mcpherson A, Gibson G, Jara H, Johann U, Luk T S, Mcintyre I A, Boyer K and Rhodes C K 1987 Studies of multiphoton production of vacuum-ultraviolet radiation in rare gases *J. Phys. B: At. Mol. Opt. Phys.* **4** 595–601

[2] Ferray M, L'Huillier A and Li X 1988 Multiple-harmonic conversion of 1064 nm radiation in rare gases *J. Phys. B: At. Mol. Opt. Phys.* **21** L31–5

[3] Constant E, Garzella D, Breger P, Mével E, Dorrer C, Le Blanc C, Salin F and Agostini P 1999 Optimizing high harmonic generation in absorbing gases: model and experiment *Phys. Rev. Lett.* **82** 1668–71

[4] Haarlammert T and Zacharias H 2009 Application of high harmonic radiation in surface science *Curr. Opin. Solid State Mater. Sci.* **13** 13–27

[5] Billaud P *et al* 2012 Molecular frame photoemission in dissociative ionization of H2 and D2 induced by high harmonic generation femtosecond XUV pulses *J. Phys. B: At. Mol. Opt. Phys.* **45** 194013

[6] Saraceno C *et al* 2013 Cutting-edge high-power ultrafast thin disk oscillators *Appl. Sci.* **3** 355–95

[7] Russbueldt P, Mans T, Rotarius G, Weitenberg J, Hoffmann H D and Poprawe R 2009 400 W Yb:YAG Innoslab fs-amplifier *Opt. Express* **17** 12230–45

[8] Eidam T, Hanf S, Seise E, Andersen T V, Gabler T, Wirth C, Schreiber T, Limpert J and Tünnermann A 2010 Femtosecond fiber CPA system emitting 830 W average output power *Opt. Lett.* **35** 94

[9] Seaberg M D *et al* 2011 Ultrahigh 22 nm resolution coherent diffractive imaging using a desktop 13 nm high harmonic source *Opt. Express* **19** 22470–9

[10] Lindner F, Stremme W, Schätzel M, Grasbon F, Paulus G, Walther H, Hartmann R and Strüder L 2003 High-order harmonic generation at a repetition rate of 100 kHz *Phys. Rev.* A **68** 013814

[11] Heyl C, Güdde J, L'Huillier A and Höfer U 2012 High-order harmonic generation with μJ laser pulses at high repetition rates *J. Phys. B: At. Mol. Opt. Phys.* **45** 074020

[12] Chiang C-T, Blättermann A, Huth M, Kirschner J and Widdra W 2012 High-order harmonic generation at 4 MHz as a light source for time-of-flight photoemission spectroscopy *Appl. Phys. Lett.* **101** 071116

[13] Merdji H, Kovačev M, Boutu W, Salières P, Vernay F and Carré B 2006 Macroscopic control of high-order harmonics quantum-path components for the generation of attosecond pulses *Phys. Rev.* A **74** 1–8

[14] Vernaleken A *et al* 2011 Single-pass high-harmonic generation at 20.8 MHz repetition rate *Opt. Lett.* **36** 3428–3340

[15] Boullet J, Zaouter Y, Limpert J, Petit S, Mairesse Y, Fabre B, Higuet J, Mével E, Constant E and Cormier E 2009 High-order harmonic generation at a megahertz-level repetition rate directly driven by an ytterbium-doped-fiber chirped-pulse amplification system *Opt. Lett.* **34** 1489–91

[16] Hädrich S, Krebs M, Rothhardt J, Carstens H, Demmler S, Limpert J and Tünnermann A 2011 Generation of μW level plateau harmonics at high repetition rate *Opt. Express* **19** 19374

[17] Hädrich S, Rothhardt J, Krebs M, Tavella F, Willner A, Limpert J and Tünnermann A 2010 High harmonic generation by novel fiber amplifier based sources *Opt. Express* **18** 20242–50

[18] Fuchs S *et al* 2013 Sensitivity calibration of an imaging extreme ultraviolet spectrometer-detector system for determining the efficiency of broadband extreme ultraviolet sources *Rev. Sci. Instrum.* **84** 023101

[19] Cabasse A, Machinet G, Dubrouil A, Cormier E and Constant E 2012 Optimization and phase matching of harmonic generation at high repetition rate *Opt. Lett.* **37** 4618–20

[20] Siegmann A E 1986 *Lasers* (Sausalito, CA: University Science Books)

[21] Lewenstein M, Salieres P and L'Huillier A 1995 Phase of the atomic polarization in high-order harmonic generation *Phys. Rev.* **52** 4747–54

[22] Popmintchev T, Chen M-C, Bahabad A, Gerrity M, Sidorenko P, Cohen O, Christov I P, Murnane M M and Kapteyn H C 2009 Phase matching of high harmonic generation in the soft and hard x-ray regions of the spectrum *Proc. Natl Acad. Sci. USA* **106** 10516–21

[23] Paul A, Gibson E A, Zhang X, Lytle A, Popmintchev T, Zhou X, Murnane M M, Christov I P and Kapteyn H C 2006 Phase-matching techniques for coherent soft x-ray generation *IEEE J. Quantum Electron.* **42** 14–26

[24] Henke B L, Gullikson E M and Davis J C 1993 X-ray interactions: photoabsorption, scattering, transmission, and reflection at E = 50–30 000 eV, Z = 1–92 *At. Data Nucl. Data Tables* **54** 181–342

[25] Midorikawa K, Nabekawa Y and Suda A 2008 XUV multiphoton processes with intense high-order harmonics *Prog. Quantum Electron.* **32** 43–88

[26] Miller D R 1988 Free jet sources *Atomic and Molecular Beam Methods* (Oxford: Oxford University Press)

[27] Ruf H *et al* 2013 Inhomogeneous high harmonic generation in krypton clusters *Phys. Rev. Lett.* **110** 083902

[28] Rothhardt J, Demmler S, Hädrich S, Limpert J and Tünnermann A 2012 Octave-spanning OPCPA system delivering CEP-stable few-cycle pulses and 22 W of average power at 1 MHz repetition rate *Opt. Express* **20** 10870–8

[29] Salières P, L'Huillier A and Lewenstein M 1995 Coherence control of high-order harmonics *Phys. Rev. Lett.* **74** 3776–9

[30] Ammosov M, Delone N and Krainov V 1986 Tunnel ionization of complex atoms and of atomic ions in an alternating electromagnetic field *Sov. Phys.—JETP* **64** 1191

[31] Schnürer M, Cheng Z, Hentschel M, Tempea G, Kálmán P, Brabec T and Krausz F 1999 Absorption-limited generation of coherent ultrashort soft-x-ray pulses *Phys. Rev. Lett.* **83** 722–5

[32] Marr G and West J 1976 Absolute photoionization cross-section tables for helium, neon, argon, and krypton in the VUV spectral regions *At. Data Nucl. Data Tables* **508** 497–508

[33] Heyl C M, Güdde J, Höfer U and L'Huillier A 2011 Spectrally resolved maker fringes in high-order harmonic generation *Phys. Rev. Lett.* **107** 033903

[34] Kazamias S, Douillet D, Weihe F, Valentin C, Rousse A, Sebban S, Grillon G, Augé F, Hulin D and Balcou P 2003 Global optimization of high harmonic generation *Phys. Rev. Lett.* **90** 193901

[35] West J and Morton J 1978 Absolute photoionization cross-section tables for xenon in the VUV and the soft x-ray regions *At. Data Nucl. Data Tables* **22** 103–7

[36] Krebs M, Hädrich S, Demmler S, Rothhardt J, Zaïr A, Chipperfield L, Limpert J and Tünnermann A 2013 Towards isolated attosecond pulses at megahertz repetition rates *Nature Photon.* **7** 555–9

[37] Mills A K, Hammond T J, Lam M H C and Jones D J 2012 XUV frequency combs via femtosecond enhancement cavities *J. Phys. B: At. Mol. Opt. Phys.* **45** 142001

[38] Seres E, Seres J and Spielmann C 2012 Extreme ultraviolet light source based on intracavity high harmonic generation in a mode locked Ti:sapphire oscillator with 9.4 MHz repetition rate *Opt. Express* **20** 6185–90

[39] Klenke A, Breitkopf S, Kienel M, Gottschall T, Eidam T, Hädrich S, Rothhardt J, Limpert J and Tünnermann A 2013 530 W, 1.3 mJ, four-channel coherently combined femtosecond fiber chirped-pulse amplification system *Opt. Lett.* **38** 2283–5

[40] Fuchs S, Blinne A, Rödel C, Zastrau U, Hilbert V, Wünsche M, Bierbach J, Frumker E, Förster E and Paulus G G 2012 Optical coherence tomography using broad-bandwidth XUV and soft x-ray radiation *Appl. Phys.* B **106** 789–95